coatings

MDPI

Article

Anti-Corrosive and Scale Inhibiting Polymer-Based Functional Coating with Internal and External Regulation of TiO_2 Whiskers

Chijia Wang [1], Huaiyuan Wang [1,2,*], Yue Hu [1], Zhanjian Liu [1], Chongjiang Lv [1], Yanji Zhu [1] and Ningzhong Bao [3]

1 College of Chemistry and Chemical Engineering, Northeast Petroleum University, Daqing 163318, China; wangchijia@163.com (C.W.); zhaoyiming0109@163.com (Y.H.); liuzhanjian2012@163.com (Z.L.); Lvcj0316@126.com (C.L.); jsipt@163.com (Y.Z.)
2 School of Chemical Engineering and Technology, Tianjin University, Tianjin 300072, China
3 State Key Laboratory of Materials-Oriented Chemical Engineering, Nanjing Technology University, Nanjing 210009, China; 15201000195@163.com
* Correspondence: wanghyjiji@163.com; Tel./Fax: +86-459-650-3083

Received: 21 November 2017; Accepted: 2 January 2018; Published: 9 January 2018

Abstract: A novel multi-functional carrier of mesoporous titanium dioxide whiskers (TiO_2(w)) modified by ethylenediamine tetra (methylene phosphonic acid) (EDTMPA) and imidazoline was devised in epoxy coating to improve the anti-corrosion and scale inhibition properties of metal surface. Rigorous characterization using analytical techniques showed that a mesoporous structure was developed on the TiO_2(w). EDTMPA and imidazoline were successfully grafted on the outer and inner surfaces of mesoporous TiO_2(w) to synthesize i$ETiO_2$(w). The results demonstrated that the corrosion resistance of the final i$ETiO_2$(w) epoxy coating is 40 times higher than that of the conventional unmodified OTiO_2(w) epoxy coating. The enhanced corrosion resistance of the i$ETiO_2$(w) functional coating is due to the chelation of the scaling cations by EDTMPA and electron sharing between imidazoline and Fe. Scale formation on the i$ETiO_2$(w) coating is 35 times lower than that on the unmodified OTiO_2(w) epoxy coating. In addition, EDTMPA and imidazoline act synergistically in promoting the barrier property of mesoporous TiO_2(w) in epoxy coating. It is believed that this novel, simple, and inexpensive route for fabricating functional surface protective coatings on various metallic materials will have a wide range of practical applications.

Keywords: scale inhibition; anti-corrosion; mesoporous TiO_2 whiskers; organic coatings; mild steel

1. Introduction

Due to its high strength and ductility, steel is widely used in industrial and engineering structures. However, corrosion of steel often leads to degeneration in its properties, waste of resources, safety problems, and environmental issues [1,2]. Therefore, protecting steel from corrosion has become a topic of prime importance, especially to minimize economic losses. In this context, protective coatings are one of the most convenient and widely used methods for corrosion protection [3,4]. As the outermost layer on metallic structures, protective coatings provide physical shielding and anodic protection. Traditional methods for improving coating performances are mainly concentrated on increasing the thickness of the coating or increasing the content of active metal powers and new protective fillers. The abovementioned methods would result in a significant cost increase [5,6]. In order to reduce the costs and achieve functionally acceptable performance, a new generation of high-performance protective coatings are required, which can provide long-life anti-corrosion, as well as other functions [7].

Corrosion inhibitors, which can reduce or prevent corrosion reactions between a metal surface and its storage environment, are some of the most commonly used materials to enhance the corrosion resistance of metals [8]. Most organic corrosion inhibitors contain nitrogen, phosphorus, and sulfur heterocyclic compounds that can facilitate adsorption and film formation on metallic surfaces [9]. Imidazoline and ethylenediamine tetra (methylene phosphonic acid) (EDTMPA) have been demonstrated to be effective in inhibiting Fe corrosion [10,11]. Traditionally, corrosion inhibitors and scaling inhibitors are dispersed in the solution around the metal surface [12]. However, inhibitor molecules in the solution can move away rapidly in flow systems. Thus, the contact time between the inhibitors and the metal surfaces is shortened, leading to low protection efficiency and high cost. Therefore, incorporate inhibitors within the coating is an attractive proposition. Nonetheless, directly adding the small molecule organic matter into the coatings in a simple way will reduce their mechanical strength of coatings. Hence, new carriers must be developed to make full use of the inhibitors in protection against corrosion and scaling.

Micro/nanocontainers have been a subject of great scientific and industrial interest in the fields of medical science and materials science [13]. Within coatings, containers have been used as fillers, for carrying solid substrates, and for the encapsulation of liquid agents [14]. Among the various types of micro/nanocontainers available, microcapsules are considered attractive owing to their ability to uniformly disperse mutually incompatible fluids in each another [15]. However most microcapsules show poor mechanical properties compared to the traditional inorganic fillers, which constrains industrial use of microcapsules in coatings. In addition, the microcapsule shell should disintegrate to release the encapsulated agents [16]. Layer-by-layer assembly particle systems have received intense and growing attention in the past few years, but the complex techniques required have seriously compromised their scale-up manufacturing and applications [17]. Hence, it is necessary to develop physically and chemically stable porous carriers for the surface coating industry.

Titanium dioxide (TiO_2) is a widely used solid filler in the coating industry due to its ability to absorb ultraviolet light and improve the stability and weather resistance of coatings [18,19]. With the intent of taking advantage of these features, we developed mesoporous TiO_2 whiskers (TiO_2(w)) with a large surface area, high thermal stability, and good mechanical properties [20]. Compared to the traditional porous materials such as zeolite and aluminum oxide, mesoporous TiO_2(w) is more suitable as a carrier in coatings. On the one hand, mesoporous TiO_2(w) provides better acid-base resistance than aluminum oxide, so it can increase the resistance of coating to pitting corrosion performance in acid-base solution. On the other hand, the zeolite requires complex synthesis procedures and is costly.

In this study, a novel route was developed to fabricate functional epoxy coating containing with modified functional mesoporous TiO_2(w) for steel substrates protection. The EDTMPA and imidazoline were modified on the surface of TiO_2(w). Subsequently, the modified functional mesoporous TiO_2(w) (i$ETiO_2$(w)) carriers were dispersed in a silicone–epoxy resin coating. The nonwettability, surface roughness, anti-corrosion property, salt spray tests and the scale inhibition property of the prepared coating were investigated. It is expected that this work will pave a new way to design and fabricate functional epoxy coatings for industrial applications.

2. Materials and Methods

Detailed information on the materials and the characterization method is supplied in the Supplementary Materials.

2.1. Preparation of Mesoporous TiO_2(w) Carriers

Mesoporous TiO_2(w) carriers were prepared using potassium titanate, according to a previously described method [21,22]. K_2CO_3 and $TiO_2 \cdot nH_2O$ powders were mixed and sintered at 810 °C for 2 h to create a mixture with a TiO_2/K_2O molar value of 1.9. 10 g of this product was soaked in 7 mL of distilled water at room temperature in a closed container for about seven days. Later, the product was suspended in 100 mL of 0.1 M HCl under vigorous stirring for 10 h. In the final step, the resultant titanic

acid suspension was calcined at a decomposition temperature of 500 °C to develop the mesoporous TiO_2(w) carriers.

2.2. Internal and External Regulation of Mesoporous TiO_2(w) Carriers

One gram of mesoporous TiO_2(w) was added to 10 mL of H_2O_2 solution and the mixture was agitated for 3 h on a magnetic stirrer at room temperature for oxidation to occur. Later, 1 g of the oxidized mesoporous TiO_2(w) ($OTiO_2$(w)) and 0.1 g of EDTMPA were added to a hydrothermal synthesis reactor (water injection rate 70%) and allowed to react at 80 °C for 24 h. At the end of this time period, the reaction mixture was filtered using 100 mL of deionized water. Subsequently, 1 g of the dried EDTMPA-grafted mesoporous TiO_2(w) ($ETiO_2$(w)) and 0.1 g of imidazoline were added to 1 mL of deionized water in a beaker and aged for 12 h. After the aged mixture was dried at 80 °C for 12 h, the imidazoline dipped $ETiO_2$(w) ($iETiO_2$(w)) was obtained.

2.3. Preparation of the Functional Epoxy Coatings

Eight grams of an organosilicon epoxy resin and 2 g of the carriers ($OTiO_2$(w) or $ETiO_2$(w) or $iETiO_2$(w)) were ultrasonically dispersed in 10 mL of ethyl acetate for 2 h. Subsequently, the coatings were prepared by spraying the ultrasonically dispersed solutions on as-treated steel plates (Q235, 80 mm × 80 mm × 1 mm) at a pressure of 0.6 MPa and curing at 180 °C for 2 h (manufacturers recommend). All the prepared coatings had an average thickness of 250 μm.

3. Results

In order to identify the composition of the synthesized functional carriers, Fourier transform infrared spectroscopy (FTIR) analysis of $OTiO_2$(w), $ETiO_2$(w), $iETiO_2$(w), and imidazoline was carried out and the resultant spectra are shown in Figure 1a. $OTiO_2$(w) exhibits four characteristic absorbance peaks, which are consistent with the reported functional groups on the surface of the as-received TiO_2(w). The band at 3432 cm^{-1} can be assigned to the –OH stretching vibration [23]. The band observed at 937 cm^{-1} is characteristic of the C–P functional group. The peak at 1165 cm^{-1} is ascribed to the scissoring motion of P=O. The band at 1365 cm^{-1} is associated with the methyl group and the band at 1637 cm^{-1} is ascribed to C–H stretching [24]. Compared with the spectrum of $OTiO_2$(w), the FTIR spectrum of $ETiO_2$(w) powder displays a sharper peak of greater intensity at 3430 cm^{-1} due to the presence of hydroxyl groups in EDTMPA. These observations confirm the presence of EDTMPA on the surface of $ETiO_2$(w). As we described in the experimental section, $ETiO_2$(w) was filtered using 100 mL deionized water in order to remove any unreacted EDTMPA. Therefore, the FTIR results indicate that EDTMPA has been successfully grafted on the $OTiO_2$(w) surface. Furthermore, no differences could be observed in the FTIR spectra of $iETiO_2$(w) and $ETiO_2$(w), which indicates that EDTMPA exists only on the surface of the $iETiO_2$(w) carrier and the imidazoline in $iETiO_2$(w) is proved to be infused into the pores of TiO_2(w).

The textural properties of the $OTiO_2$(w), $ETiO_2$(w), and $iETiO_2$(w) multi-functional carriers, including their Brunauer-Emmett-Teller (BET) surface areas, pore volumes, and pore diameters are summarized in Table 1. The BET surface area, total pore volume, and average pore diameter of $OTiO_2$(w) are 52.37 m^2/g, 0.12 cm^3/g, and 9.2 nm, respectively. As reported elsewhere, the BET surface area of traditional TiO_2 systems, such as P25, is approximately 10 m^2/g [25]. The high BET surface area of $OTiO_2$(w) is attributed to the whisker morphology and the numerous pores on the surface (as shown in Figure 2a). After the incorporation of EDTMPA, the S_{BET} of $OTiO_2$(w) decreased slightly, indicating that EDTMPA is dispersed on the surface of $OTiO_2$(w), which agrees well with the FTIR and X-ray diffraction (XRD) results. Moreover, upon being impregnated by imidazoline, the S_{BET} of $iETiO_2$(w) decreased dramatically to 32.53 m^2/g. These results demonstrate that the internal pores of TiO_2(w) were partly filled by imidazoline.

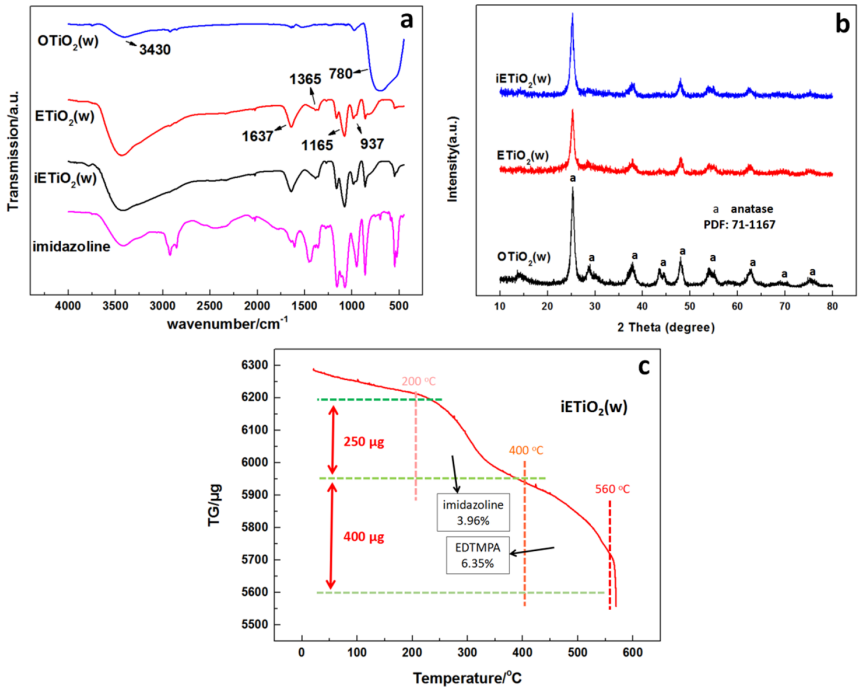

Figure 1. (**a**) FTIR spectra of $OTiO_2$(w), $ETiO_2$(w), $iETiO_2$(w), and imidazoline; (**b**) XRD patterns of $OTiO_2$(w), $ETiO_2$(w), and $iETiO_2$(w); (**c**) Thermogravimetric (TG) analysis curve of $iETiO_2$(w).

Table 1. Textural and structural properties of the multi-functional carriers.

Sample	S_{BET} (m^2/g)	V_p (cm^3/g)	Average Pore Diameter (nm)
$OTiO_2$(w)	52.37 ± 0.26	0.120 ± 0.006	9.2
$ETiO_2$(w)	48.74 ± 0.25	0.100 ± 0.005	8.2
$iETiO_2$(w)	32.53 ± 0.16	0.060 ± 0.003	7.4

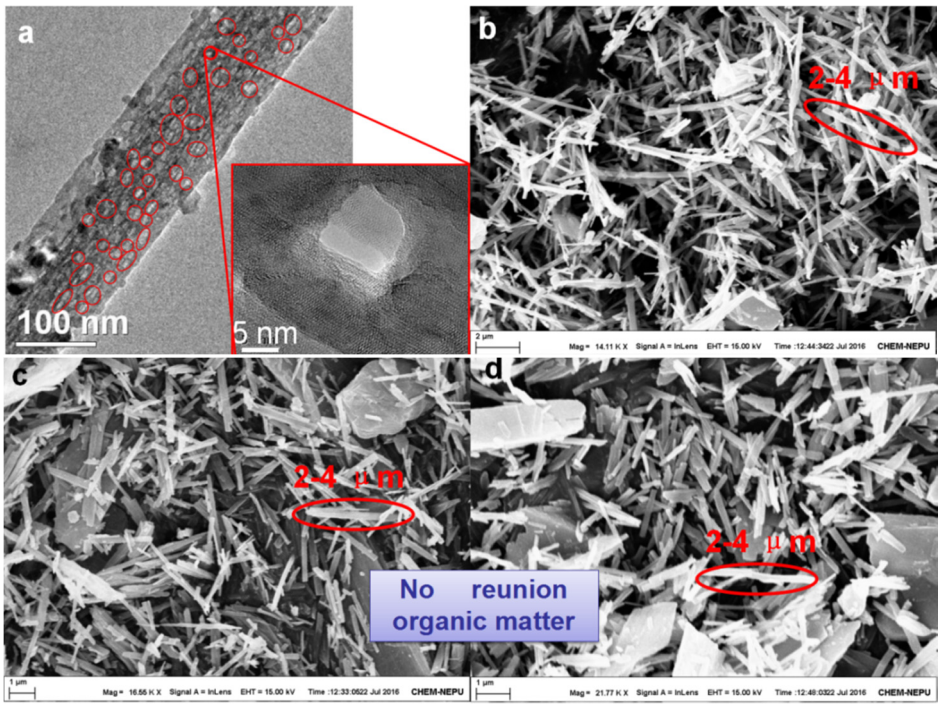

Figure 2. TEM image (**a**) of $OTiO_2$(w), SEM images of (**b**) $OTiO_2$(w), (**c**) $ETiO_2$(w), and (**d**) $iETiO_2$(w).

The thermal stability of $iETiO_2$(w) was studied using a thermogravimetry (TG) analyzer to confirm the existence of imidazoline. As shown in Figure 1c, there is a small weight loss at temperatures below 200 °C due to the volatilization of water. In the second thermal event between 200 °C and 400 °C, $iETiO_2$(w) loses about 250 μg (4% of its total mass) because of the oxidative decomposition of imidazoline [26]. Since imidazoline is absorbed into the pores on the whisker and linked to the inner surface of titanium dioxide via chemical bonds, it results in an increase in the oxidation decomposition temperature of imidazoline. The final thermal event in the TG curve is a representative of the EDTMPA decomposition diagram [27].

The crystalline phases in the multi-functional carriers were determined by XRD analysis. Figure 1b depicts the XRD patterns of $OTiO_2$(w), $ETiO_2$(w), and $iETiO_2$(w). The diffraction peaks of the anatase TiO_2 phase (PDF: 71-1167) can be identified in all the samples. The XRD results show that the TiO_2(w) crystal did not change after the oxidation and hydrothermal treatments. Moreover, apart from the peak related to anatase, no other peak could be observed in the three patterns, indicating that EDTMPA and imidazoline are evenly dispersed on the surface or inside the pores of $OTiO_2$(w). From the FTIR, XRD, TG, and BET results, it can be concluded that EDTMPA is spread on the outer surfaces of the mesoporous TiO_2(w) carriers while imidazoline is loaded in the internal pores of the mesoporous TiO_2(w) carriers.

In order to analyze the morphologies of the multi-functional carriers, scanning electron microscopy (SEM) was carried out. The SEM images of $OTiO_2$(w) and the modified mesoporous TiO_2(w) are displayed in Figure 2. The whisker shape of TiO_2(w) can be observed in Figure 2b; a large number of TiO_2 whiskers with an average diameter of 100 nm and an average length of 3 μm were evenly distributed throughout the sample. Interestingly, the transmission electron microscopy (TEM) image shows that there exist nano-sized pores (with an average diameter of 9.2 nm) on the surface of mesoporous TiO_2(w) (Figure 2a) and the representative pores have been marked. Figure 2c displays the surface morphology of $ETiO_2$(w). As shown in the image, there was no reunion of $ETiO_2$(w) with the organic matter and the morphology of the whisker remains unchanged even after the hydrothermal reaction. The morphology of the whiskers after immersion in imidazoline is shown in Figure 2d; the whiskers maintain their original morphological characteristics. The SEM results show that functional processing did not alter the pristine whisker morphology; EDTMPA and imidazoline are evenly dispersed on the exterior surface and the internal pores of the functional $iETiO_2$(w) carriers. These results are in good agreement with the FTIR observations.

The chemical modification mechanisms of imidazoline and EDTMPA on mesoporous TiO_2(w) are schematically illustrated in Figure 3. A large number of high-activity hydroxyl groups are generated on the surface of mesoporous TiO_2(w) after oxidation with H_2O_2. EDTMPA is a tetramethylene compound with four phosphate groups in its molecular structure. A hydroxyl group on the $OTiO_2$(w) surface and one of the phosphate groups of EDTMPA react under hydrothermal conditions. Its complex molecular structure and short chains make it difficult for EDTMPA to react with four hydroxyl groups at the same time. The phosphate groups that are not involved in the reaction serve as the scale inhibiting functional groups [28]. After the EDTMPA reaction, imidazoline groups are infused into the pores on the whiskers by immersion. The nitrogen in the imidazoline molecule has a lone pair of electrons in its outer shell. On the other hand, Ti^{4+} of mesoporous TiO_2(w) has an unsaturated 3d shell, which can accommodate two electrons [29]. Thus the corrosion inhibitor is deposited on the inner surface of the whisker under the dual action of physical and chemical adsorption. The results of specific surface characterization of different samples support the modification mechanisms described above.

Figures 4 and 5 present the EIS spectra of pure epoxy coating and the epoxy coatings containing $OTiO_2$(w) and $iETiO_2$(w), the spectra were obtained during long-term immersion conditions. The deterioration process of the pure epoxy coating can be divided into two stages (Figure 4a). During the first day, the coating exhibited a strong barrier effect, as indicated by the single large capacitive arc. The Nyquist plot of the spectra from seven to 60 days contained two time-constant semicircles, which are regarded as the capacitive loops, at medium and low frequencies. The medium

frequency capacitive loops related to the charge transfer of corrosion reaction at the electrode surface. The loop at low frequencies is attributed to the charge transfer resistance (R_{ct}). These results indicate the permeation of oxygen, water, and corrosive ions (Cl^-) through the epoxy coating, finally resulting in under-film corrosion and coating delamination [30,31].

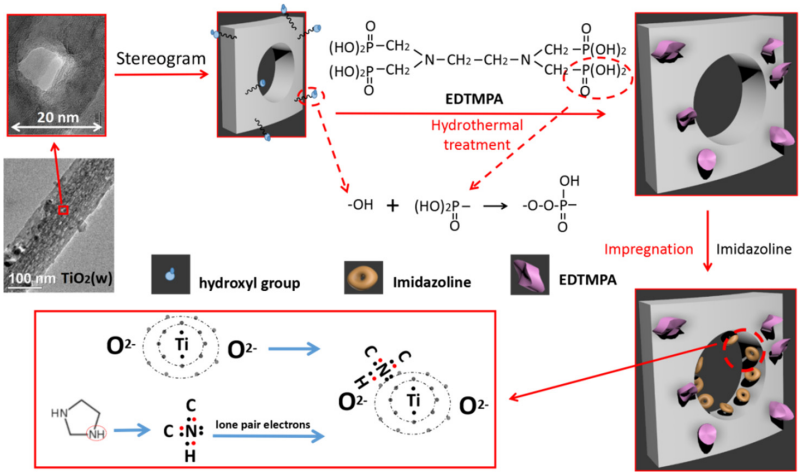

Figure 3. Modification of the carriers by EDTMPA and imidazoline.

The Nyquist plots (Figure 4b) constructed from the EIS spectra of the $OTiO_2$(w) epoxy coating were characterized by two large capacitive arcs from one to 60 days of immersion. The first arc corresponds to the capacitive impedance of the coating, which is measured by the diameter of the semicircles and the second arc corresponds to the polarization resistance process at the steel surface beneath the coating layer [32]. During the curing and application processes, many defects, such as micro-porosities, cavities, as well as free volumes are generated in the coating, resulting in the corrosive electrolyte penetrating into the coating matrix and leading to coating's degeneration and reduction of barrier performance [33].

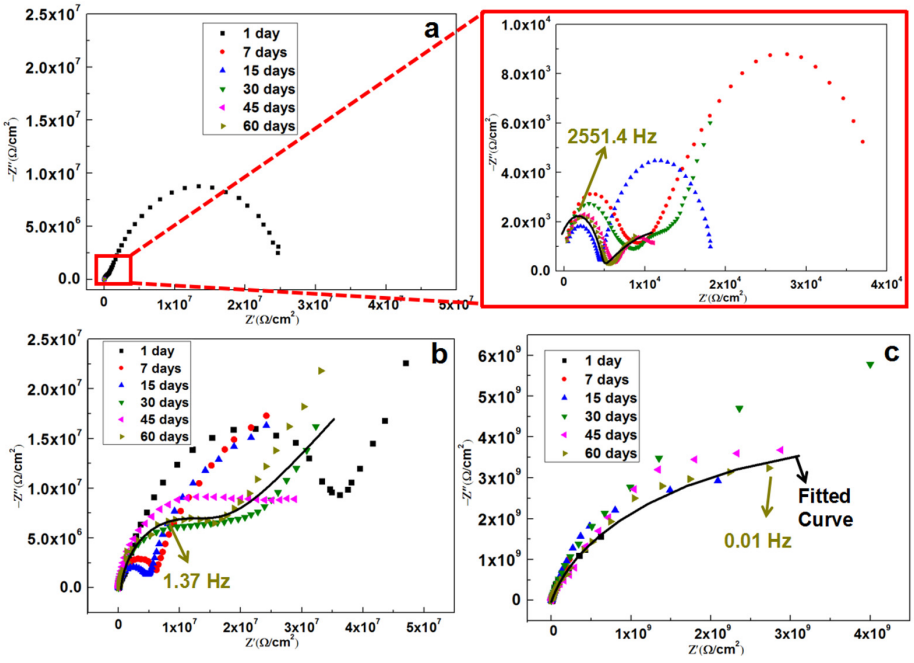

Figure 4. Nyquist plots of (**a**) pure epoxy coating, (**b**) $OTiO_2$(w) epoxy coating, (**c**) and $iETiO_2$(w) epoxy coating.

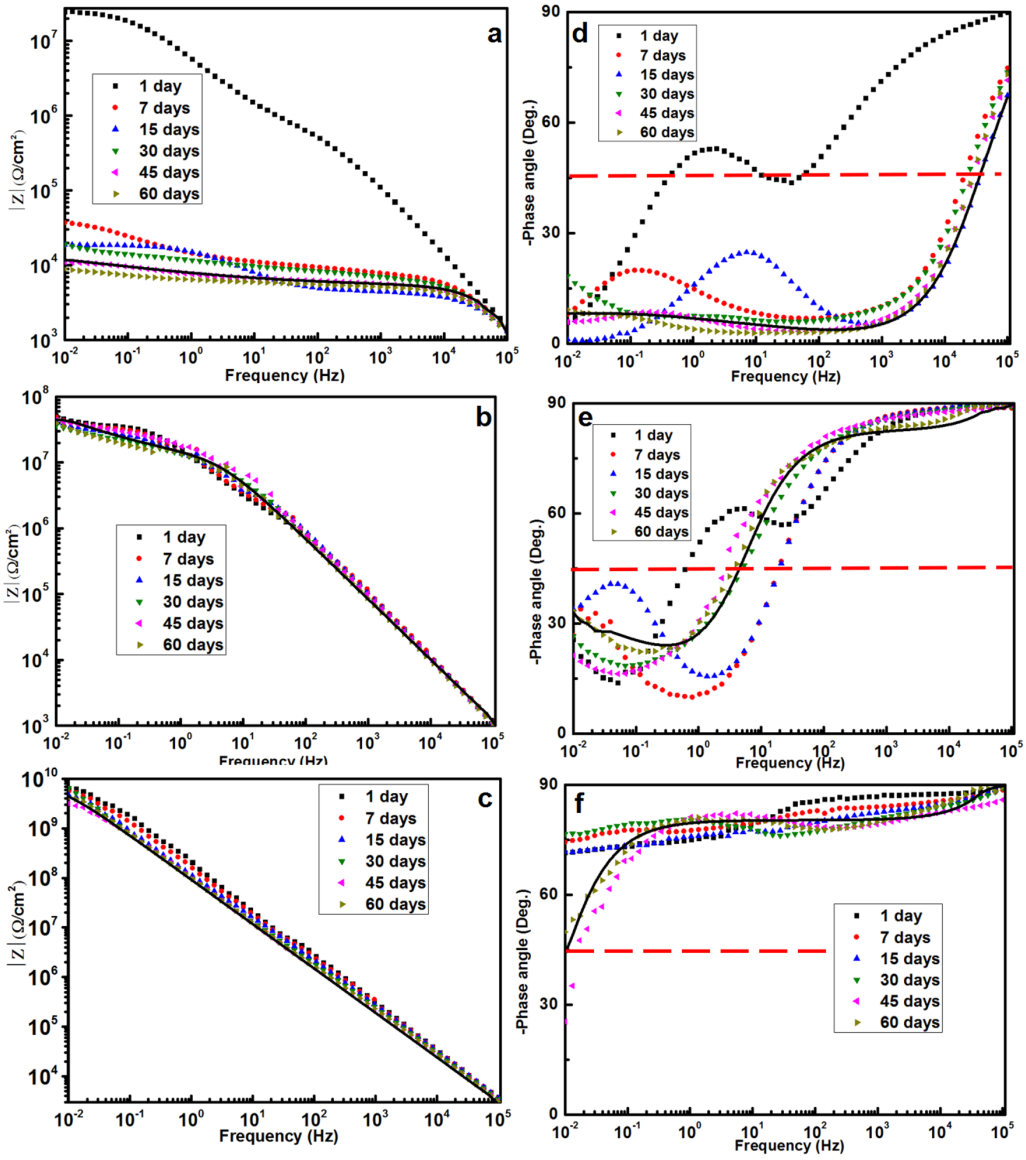

Figure 5. Bode plots of (**a**,**d**) pure epoxy coating, (**b**,**e**) OTiO$_2$(w) epoxy coating, and (**c**,**f**) iETiO$_2$(w) epoxy coating.

Furthermore, the long-term anti-corrosion performance of the iETiO$_2$(w) epoxy coating can be deciphered from Figure 4c. It can be seen that the diameter of the semicircle is about 8×10^8 Ω/cm^2 at day 1. Interestingly, as time goes by, the semicircle diameter starts to grow up to 10^9 Ω/cm^2, which indicates that the capacitive impedance of the coating can be increased by soaking it in a NaCl solution. At day 45, the semicircle diameter begins to reduce. This phenomenon is caused by the inhibitors activated by water molecules penetrate into the coating. Furthermore, the Nyquist plots for the iETiO$_2$(w) epoxy coating exhibit one semicircle over the whole frequency range during the 60 days exposure period, indicating a capacitive behavior and barrier type protection.

By using Bode plots, the barrier performance of the coatings was semi-quantitatively measured in terms of the impedance modulus at the lowest frequency ($|Z|_{0.01\ Hz}$) [34]. In Figure 5a, the Bode plot for day 1 is a straight line, with a low-frequency impedance modulus that reaches a value of 10^7 Ω/cm^2. After seven or more days of immersion, overlapping straight lines can be observed with a low-frequency impedance modulus of ~10^5 Ω/cm^2, which is typical for epoxy coatings in harsh degeneration conditions [35]. The phase diagram confirms that there are already two time

constants after one day of immersion, which might be associated with the electrochemical double layer capacitance on the solid/electrolyte interface. In Figure 5b, the $|Z|_{0.01\,Hz}$ values remain steady at $5 \times 10^7\ \Omega/cm^2$ after 60 days of immersion. This result points out that $OTiO_2$(w) can greatly improve the shielding effectiveness of the epoxy coating.

The breakpoint frequency (BF, frequency at 45° phase angle) values can also be obtained from the Bode diagrams. BF reflects the evolution of delamination and corrosion products beneath the coating. It can be observed from the phase diagram that the BF of pure epoxy is 100 Hz, while that of $OTiO_2$(w) epoxy coating is at about 1 Hz. The BF value decreases with an increase in the modified depth of the coating. A lower plateau is seen at low frequencies, the phase diagrams are all characteristic with two time constants, and higher breakpoint frequencies were observed in Figure 5d–f, indicating a continuous decrease in the barrier properties during the immersion period for the pure epoxy coating and $OTiO_2$(w) epoxy coating. Comparatively, the long-term anti-corrosion performance of the $iETiO_2$(w) epoxy coating can also be reflected by the stable $|Z|_{0.01\,Hz}$ values and high phase angles (~70°) over a wide range of frequency during the 60 days' immersion. The high phase indicates the high resistance of the coating. The above BF results are found to be in good agreement with the Nyquist plots.

In the case of the $iETiO_2$(w) epoxy coating, the $|Z|_{0.01\,Hz}$ values remained higher than $1 \times 10^9\ \Omega/cm^2$ after 60 days of immersion, indicating that it had the highest shielding performance among all the tested coatings. The Nyquist plots (Figure 4c), the Bode plots (Figure 5c), and the phase diagrams (Figure 5f) of the $iETiO_2$(w) epoxy coating indicate its pure capacitive behavior over the entire 60-day immersion period. The barrier properties remained constant despite the phase angles starting to decrease at lower frequencies at 45 and 60 days, which implies that a small amount of water penetrated into the coating [36]. The EIS results show that the barrier property of $iETiO_2$(w) epoxy coating is 20–50 times higher than that of the $OTiO_2$(w) epoxy coating. Water started penetrating into the $iETiO_2$(w) epoxy coating 45 days later than it did in the case of the unmodified pure epoxy coating.

The electronic equivalent circuits (EECs) of the EIS results are displayed in Figure 6a–c. R_c and Q_c represent the resistance and constant phase element (CPE) of the coating, respectively. The charge transfer resistance (R_{ct}) and CPE of the electric double layer (Q_{dl}) appear after corrosion takes place beneath the coating. When the corrosion products diffuse through the pores in the coating, Warburg impedance (W) is added and serialized to R_{ct} [37,38]. The EEC shown in Figure 6a is used to fit the spectra of the $iETiO_2$(w) epoxy coating from 0 to 60 days of immersion, during which no corrosion signals could be detected from underneath the coatings (Figure 7c). Figure 6b is related to the $OTiO_2$(w) epoxy coating from one to 60 days of immersion (Figure 7b) and the pure epoxy coating during one day of immersion. It appears that the water molecules invaded the pure epoxy coating, leading to the corrosion of steel. In the case of a pure epoxy coating immersed for more than seven days, corrosion inducers diffused into the coating surface (Figure 7a). Therefore, Figure 6c conforms to the EEC of the pure epoxy coating from seven to 60 days of immersion. The fitting lines of the three coatings after immersion in 3.5 wt % NaCl solution for 60 days are shown in Figures 4 and 5. Results show that the black lines (fitting lines) are consistent with the trend of the dark green triangle, which means that the EECs are conforming to the circuit situation of each coating in a 3.5 wt % NaCl solution.

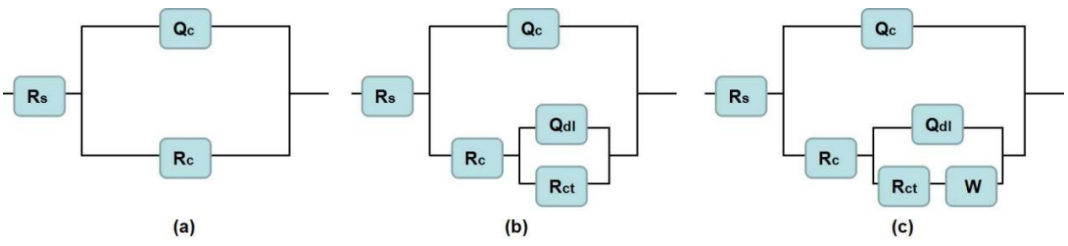

Figure 6. Electrical equivalent circuits used for fitting the EIS spectra. (**a**) one time constants equivalent circuits, (**b**,**c**) two time constants equivalent circuits.

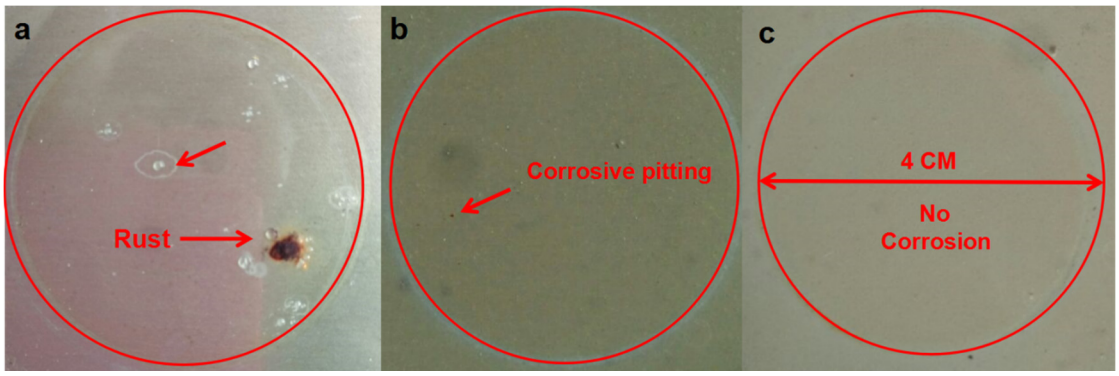

Figure 7. Surface topography of (**a**) pure epoxy coating, (**b**) $OTiO_2$(w) epoxy coating, and (**c**) $iETiO_2$(w) epoxy coating after ESI measurement.

Table 2 summarizes the results of the fitted parameters of the three coatings after immersion in 3.5 wt % NaCl solution for 60 days. It is evident that the R_t (R_t means $R_c + R_{ct}$) values of the pure epoxy coating are a thousand times smaller than those of the $OTiO_2$(w) epoxy coating. This observation indicates that the corrosion resistance of the pure epoxy coating deteriorated completely over 60 days. The R_t values of the $OTiO_2$(w) epoxy coating after 60 days of immersion are still very high. Interestingly, the R_t of the $iETiO_2$(w) epoxy coating is 40 times higher than that of the $OTiO_2$(w) epoxy coating. It should be noted that the CPE exponents (n_1) for all coatings at about 0.9. Q_c values are considered approximations of pure capacitances. The higher Rt and lower Q_c also contributed to the outstanding barrier property of the $iETiO_2$(w) epoxy coating. Results of the fitted parameters are in accordance with the Nyquist and Bode plots.

Table 2. Fitting parameters to simulate the EIS data of the pure epoxy coating, $OTiO_2$(w) epoxy coating, and $iETiO_2$(w) epoxy coating after immersion in 3.5 wt % NaCl solution for 60 days.

Coating	R_c	Q_c		R_{ct}	Q_{dl}	
	Ω cm^2	$Y_1 \times 10^{-9}$ (Ω^{-1} cm^{-2} s^n)	n_1	Ω cm^2	$Y_2 \times 10^{-6}$ (Ω^{-1} cm^{-2} s^n)	n_2
Pure epoxy coating	5531.8 ± 108	6.23 ± 0.15	0.86 ± 0.04	16,526 ± 400	201 ± 4	0.26 ± 0.01
$OTiO_2$(w) epoxy coating	1.19×10^6	3.86 ± 0.09	0.92 ± 0.05	1.20×10^8	0.076 ± 0.005	0.43 ± 0.02
$iETiO_2$(w) epoxy coating	8.96×10^9	1.91 ± 0.05	0.89 ± 0.05	–	–	–

It can be seen from the results described above that the impedance values of the pure epoxy coating and the $OTiO_2$(w) epoxy coating decreased with the increase of immersion time. This means that the corrosive electrolyte gradually diffused into the two coatings, while it is obvious that the inclusion of $iETiO_2$(w) had a significant impact on the epoxy coating's corrosion protection performance. The corrosion improving mechanism of the epoxy coating will be discussed in the following sections.

In order to further determine the long-term anti-corrosion properties of the coatings, accelerated corrosion tests were conducted in a neutral salt spray using a 5 wt % NaCl solution as the corrosive medium. Figure 8 shows the appearance of the four samples after 45 days of salt spray testing. Severe corrosion occurs on the pure epoxy coating. The brick red corrosion products are attributed to the formation of iron oxide. The red rust exists not only along the scratches but also spreads out to the unscratched coated surface. The above phenomenon is attributed to the poor protective and isolation performance of the pure epoxy coating. It can be seen from Figure 8b that the corrosion products exist mainly on the scratched area of the coating surface and no visible corrosion products can be seen on the unscratched surface. This indicates that the addition of $OTTiO_2$(w) can effectively prevent water molecules and chloride ions from penetrating through the coating, thus improving the protective performance of the epoxy coating. Different from the above results, it is evident from

Figure 8c that the iETiO$_2$(w) epoxy coating exhibits outstanding corrosion resistance during the whole salt spray test. No obvious brick red corrosion products are formed on the scratches or the other outer surface. The results show that the corrosion inhibitor encapsulated in the multi-functional carrier is released when water molecules penetrate into the coating. Figure 8d shows the salt spray test results of a commercial anti-corrosion coating (Rust Bullet) used as the reference sample. It can be understood from the salt spraying test results that the adhesion and corrosion resistance of the iETiO$_2$(w) epoxy coating are much higher than those of the commercial coating.

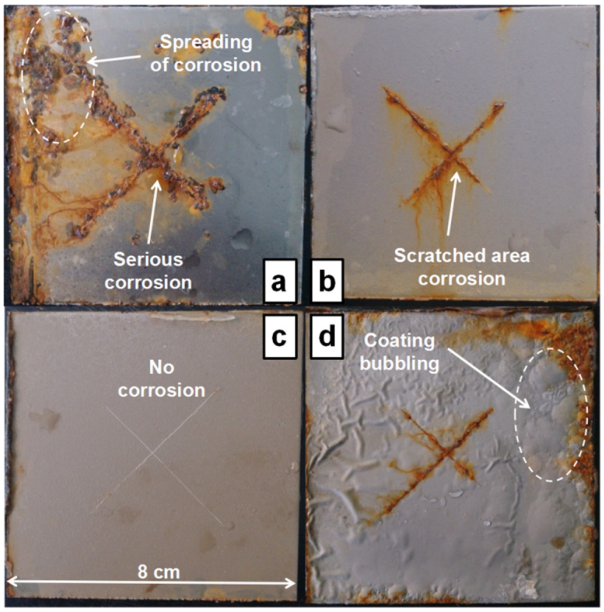

Figure 8. Salt spray tests results of (**a**) pure epoxy coating, (**b**) OTiO$_2$(w) epoxy coating, (**c**) iETiO$_2$(w) epoxy coating, (**d**) a commercial anti-corrosion coating (Rust Bullet).

In addition, electrochemical measurement for the defective iETiO$_2$(w) epoxy coating and the defected epoxy coating after 24 h salt spray tests is shown in Figure S1. The Nyquist plots (Figure S1a) constructed from the EIS data for the two defected coating were characterized by one large capacitive arc after 24 h salt spray tests. Both of the Bode plots exhibit a slight decline in the low-frequency range (Figure S1b). The phase diagram shows that there are already two evident time constants at 24 h of salt spraying, which confirms that the steel plates are exposed to the NaCl solution (Figure S1c). Furthermore, the capacitive arcs visible in the Nyquist plot and the value of $|Z|_{0.01\ \mathrm{Hz}}$ (as shown in Figure S1) indicates that the charge transfer between the metal and the solution is hindered, which means that the iETiO$_2$(w) epoxy coating has a higher anti-corrosion performance.

Figure 9 illustrates the surfaces of coatings after being immersed in a $CaCl_2/NaHCO_3$ solution for 72 h. It can be seen that the surfaces of the pure epoxy coating and OTiO$_2$(w) epoxy coating are covered with a large number of cube-like blocks with an average size of 8 μm (Figure 9a,c). XRD analysis of the surface of the pure epoxy coating (Figure 9c) reveals that the cube-like entities are mainly the products of $CaCO_3$ fouling. Interestingly, Figure 9d reveals that there is very little $CaCO_3$ scaling on the surface of the multi-functional iETiO$_2$(w) epoxy coating [39]. In order to measure the scaling rate of the samples, the SEM images are converted to black and white two-value pictures. The gray value of the fouling material in the binary image is 255 and that of the others are 0. Finally, the scaling rate is obtained by calculating the proportion of 255 in the data. The results show that the scaling rates of the pure epoxy coating, OTiO$_2$(w) epoxy coating, and the iETiO$_2$(w) epoxy coating are 43%, 41.5%, and 1.2%, respectively. The scale formation on the iETiO$_2$(w) epoxy coating is 35 times lower than that on the OTiO$_2$(w) epoxy coating. The good scale inhibition effect of the iETiO$_2$(w) epoxy coating is obvious from the SEM analysis and the scale formation test.

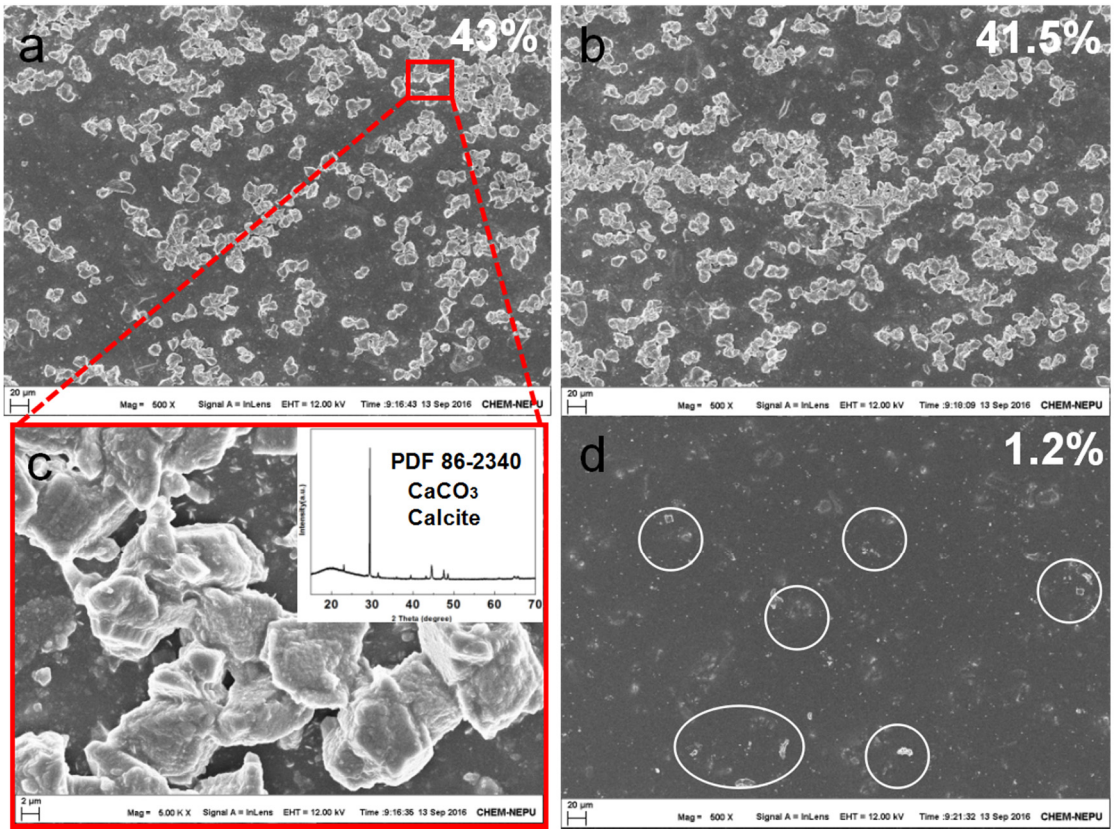

Figure 9. Scale inhibition property of (**a**,**c**) pure epoxy coating, (**b**) $OTiO_2$(w) epoxy coating, and (**d**) $iETiO_2$(w) epoxy coating.

The roughness data and pictures of the contact angle of pure epoxy coating, $OTiO_2$(w) epoxy coating, and $iETiO_2$(w) epoxy coating are shown in Figure 10. It can be seen from the pictures that the difference in roughness between the three samples is small. The pure epoxy coating is a smoother coating, with a contact angle at 98°. The roughness is improved and the contact angle is reduced to 80° when $OTiO_2$(w) is added to the coating. Although the roughness of the two epoxy coatings filled with TiO_2(w) is almost the same, the contact angle of the $iETiO_2$(w) epoxy coating is higher than the $OTiO_2$(w). The above phenomenon is mainly due to the –OH, which is hydrophilic, on the surface of $OTiO_2$(w). There are many fewer hydrophilic groups on the surface of $iETiO_2$(w) after surface modification. The improvement of the roughness of the coatings is mainly caused by adding fillers (TiO_2(w)) to the coating. The results above also demonstrated that the functional groups on the surface of the fillers can be exposed to the coating surface.

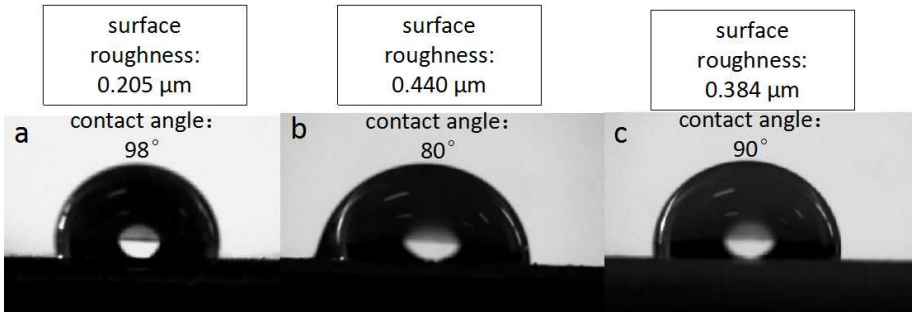

Figure 10. The roughness data and picture of contact angle of (**a**) pure epoxy coating, (**b**) $OTiO_2$(w) epoxy coating, and (**c**) $iETiO_2$(w) epoxy coating.

4. Discussion

Based on the chemical composition and characterization results described above, the anti-corrosion and scale inhibition mechanisms of the three coatings are discussed here. It has been shown in Figure 3 that the EDTMPA is a molecule containing four anti-scaling functional groups. When one phosphate group of EDTMPA is connected to one hydroxide radical on the surface of mesoporous TiO_2(w), the other unreacted anti-scaling functional groups are exposed to the outer surface, which can be used to bind cations. Then the scaling cations, such as Ca^{2+} and Mg^{2+}, will chelate with the anti-scaling functional groups, eventually leading to the formation of HCO_3^-, which cannot precipitate due to the lack of scaling cations (Figure 11) [40]. Meanwhile, there would always be EDTMPA exposed on the outer surface on the i$ETiO_2$(w) epoxy coating, even if the coating undergoes abrasion or breakage, since the functionalized i$ETiO_2$(w) is evenly dispersed in the epoxy coating.

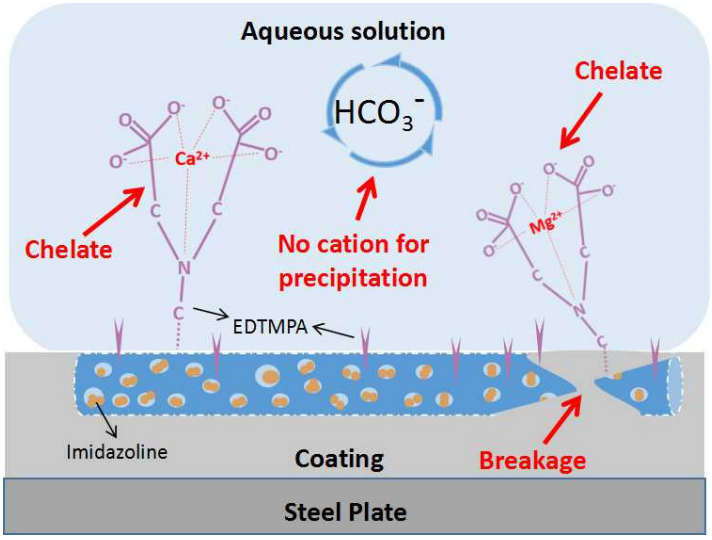

Figure 11. The scale inhibition mechanism of an i$ETiO_2$(w) epoxy coating.

The corrosion protection mechanism of the i$ETiO_2$(w) coating is displayed in Figure 12. It can be seen that the anti-corrosion process is divided into two steps. As displayed in the morphology section, mesoporous TiO_2(w) have an average diameter of 100 nm and an average length of 3 μm. When the water molecules permeate into the coating, mesoporous TiO_2(w) will obstruct the water molecules from directly penetrating into the coating/metal interface. After a long immersion or when the coating is scratched, water molecules reach the coating/metal interface (step 2); then imidazoline is activated by the water molecules and forms self-assembled monolayers on iron substrates, which also prevents rusting [41].

In summary, the barrier performance of the i$ETiO_2$(w) epoxy coating can be enhanced by the synergistic effect of EDTMPA and imidazoline. Compared to the traditional epoxy-based anti-corrosive coatings, the i$ETiO_2$(w) coating has the strongest anti-scaling and anti-corrosion properties. In consequence, using our particular experimental design, the processes of scale inhibition and corrosion inhibition can be mutually promoted.

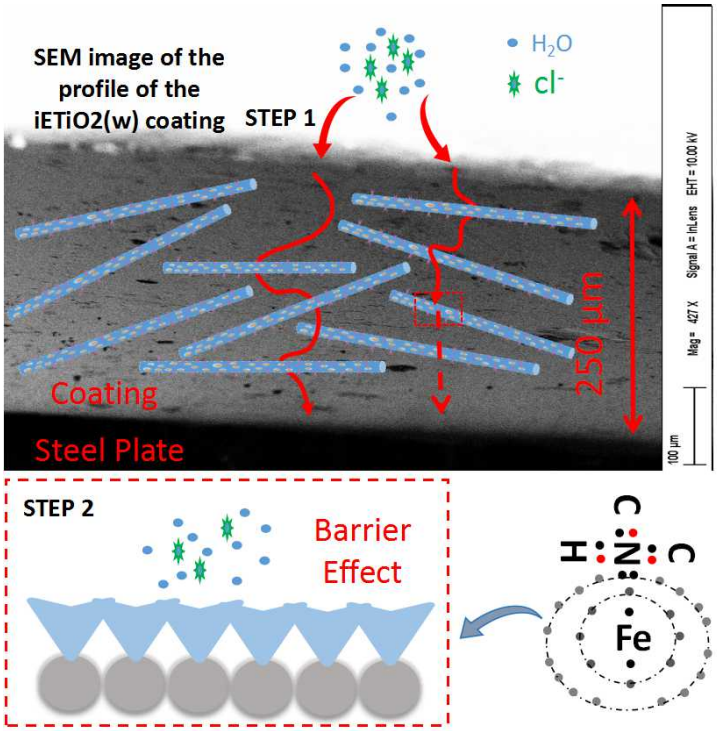

Figure 12. The corrosion protection mechanism of an iETiO$_2$(w) epoxy coating.

5. Conclusions

We have successfully fabricated a novel, multi-functional epoxy coating with outstanding scale and corrosion prevention properties for steel substrates by internally and externally regulating mesoporous TiO$_2$(w). The functional inhibitors imidazoline and EDTMPA modified the surface of mesoporous TiO$_2$(w), as evidenced by FTIR, TG, and BET analyses. The coatings were investigated for non-wettability, surface roughness, and anti-corrosion properties using salt spray tests and the scale inhibition. The main conclusions that could be drawn from our results are as follows:

- Analysis by electrochemical impedance spectroscopy showed that the resistance of the iETiO$_2$(w) epoxy coating exhibited outstanding barrier properties with a high resistance (8.96×10^9 Ω/cm^2) and long protection time, which indicates that the iETiO$_2$(w) epoxy coating exhibited excellent corrosion protection performance.
- Scale formation on the iETiO$_2$(w) epoxy coating was found to be 35 times lower than on the unmodified mesoporous TiO$_2$(w) epoxy coating, which means that the EDTMPA modified on the surface of the iETiO$_2$(w) plays an key role in the scale inhibition of the coating.

We believe that this novel route to fabricate anti-corrosion and scale-inhibiting coatings will inspire large-scale practical surface protection of structures such as steel pipelines, vessels, ships, and marine drilling platforms.

Supplementary Materials: The Supplementary Materials are available on http://www.mdpi.com/2079-6412/8/1/29/s1.

Acknowledgments: This research was financially supported by the National Young Top Talents Plan of China (2013042), the National Science Foundation of China (21676052, 21606042), the Northeast Petroleum University Innovation Foundation for Postgraduates (YJSCX2016-016NEPU), and the State Key Laboratory of Materials-Oriented Chemical Engineering (KL15-11).

Author Contributions: Chijia Wang and Huaiyuan Wang conceived and designed the experiments; Chijia Wang and Yue Hu performed the experiments; Zhanjian Liu, Chongjiang Lv, and Yanji Zhu analyzed the data; Chijia Wang, Huaiyuan Wang, and Ningzhong Bao wrote the paper.

Conflicts of Interest: The authors declare no conflict of interest.

References

1. Liu, T.; Yin, Y.; Chen, S.; Chang, X.; Cheng, S. Super-hydrophobic surfaces improve corrosion resistance of copper in seawater. *Electrochim. Acta* **2007**, *52*, 3709–3713. [CrossRef]
2. Merachtsaki, D.; Xidas, P.; Giannakoudakis, P.; Triantafyllidis, K.; Spathis, P. Corrosion protection of steel by epoxy-organoclay nanocomposite coatings. *Coatings* **2017**, *7*, 84. [CrossRef]
3. Barbhuiya, S.; Choudhury, M. Nanoscale characterization of glass flake filled vinyl ester anti-corrosion coatings. *Coatings* **2017**, *7*, 116. [CrossRef]
4. Wang, N.; Xiong, D.; Deng, Y.; Shi, Y.; Wang, K. Mechanically robust superhydrophobic steel surface with anti-icing, uv-durability, and corrosion resistance properties. *ACS Appl. Mater. Interfaces* **2015**, *7*, 6260–6272. [CrossRef] [PubMed]
5. Bai, N.; Li, Q.; Dong, H.; Tan, C.; Cai, P.; Xu, L. A versatile approach for preparing self-recovering superhydrophobic coatings. *Chem. Eng. J.* **2016**, *293*, 75–81. [CrossRef]
6. Banerjee, S.; Wehbi, M.; Manseri, A.; Mehdi, A.; Alaaeddine, A.; Hachem, A.; Ameduri, B. Poly (vinylidene fluoride) containing phosphonic acid as anticorrosion coating for steel. *ACS Appl. Mater. Interfaces* **2017**, *9*, 6433–6443. [CrossRef] [PubMed]
7. Liu, Y.; Liu, J. Design of multifunctional SiO_2–TiO_2 composite coating materials for outdoor sandstone conservation. *Ceram. Int.* **2016**, *42*, 13470–13475. [CrossRef]
8. Hu, K.; Zhuang, J.; Zheng, C.; Ma, Z.; Yan, L.; Gu, H.; Zeng, X.; Ding, J. Effect of novel cytosine-l-alanine derivative based corrosion inhibitor on steel surface in acidic solution. *J. Mol. Liq.* **2016**, *222*, 109–117. [CrossRef]
9. Kermannezhad, K.; Chermahini, A.N.; Momeni, M.M.; Rezaei, B. Application of amine-functionalized MCM-41 as PH-sensitive nano container for controlled release of 2-mercaptobenzoxazole corrosion inhibitor. *Chem. Eng. J.* **2016**, *306*, 849–857. [CrossRef]
10. Zhang, K.; Xu, B.; Yang, W.; Yin, X.; Liu, Y.; Chen, Y. Halogen-substituted imidazoline derivatives as corrosion inhibitors for mild steel in hydrochloric acid solution. *Corros. Sci.* **2015**, *90*, 284–295. [CrossRef]
11. Gao, Q.; Wang, S.; Luo, W.J.; Feng, Y.Q. Facile synthesis of magnetic mesoporous titania and its application in selective and rapid enrichment of phosphopeptides. *Mater. Lett.* **2013**, *107*, 202–205. [CrossRef]
12. Raja, P.B.; Sethuraman, M.G. Natural products as corrosion inhibitor for metals in corrosive media—A review. *Mater. Lett.* **2008**, *62*, 113–116. [CrossRef]
13. Cao, H.; He, J.; Deng, L.; Gao, X. Fabrication of cyclodextrin-functionalized superparamagnetic Fe_3O_4/amino-silane core–shell nanoparticles via layer-by-layer method. *Appl. Surf. Sci.* **2009**, *255*, 7974–7980. [CrossRef]
14. Shchukina, E.; Shchukin, D.; Grigoriev, D. Effect of inhibitor-loaded halloysites and mesoporous silica nanocontainers on corrosion protection of powder coatings. *Prog. Org. Coat.* **2017**, *102*, 60–65. [CrossRef]
15. Dong, B.; Wang, Y.; Fang, G.; Han, N.; Xing, F.; Lu, Y. Smart releasing behavior of a chemical self-healing microcapsule in the stimulated concrete pore solution. *Cem. Concr. Compos.* **2014**, *56*, 46–50. [CrossRef]
16. Kamburova, K.; Boshkova, N.; Boshkov, N.; Radeva, T. Design of polymeric core-shell nanocontainers impregnated with benzotriazole for active corrosion protection of galvanized steel. *Colloids Surf. A* **2016**, *499*, 24–30. [CrossRef]
17. Richardson, J.J.; Cui, J.; Björnmalm, M.; Braunger, J.A.; Ejima, H.; Caruso, F. Innovation in layer-by-layer assembly. *Chem. Rev.* **2016**, 14828–14867. [CrossRef] [PubMed]
18. Wang, H.; Zhang, S.; Wang, G.; Yang, S.; Zhu, Y. Tribological behaviors of hierarchical porous peek composites with mesoporous titanium oxide whisker. *Wear* **2013**, *297*, 736–741. [CrossRef]
19. Mazur, M.; Wojcieszak, D.; Kaczmarek, D.; Domaradzki, J.; Song, S.; Gibson, D.; Placido, F.; Mazur, P.; Kalisz, M.; Poniedzialek, A. Functional photocatalytically active and scratch resistant antireflective coating based on TiO_2 and SiO_2. *Appl. Surf. Sci.* **2016**, *380*, 165–171. [CrossRef]
20. Wang, H.; Cheng, X.; Xiao, B.; Wang, C.; Li, Z.; Zhu, Y. Surface carbon activated NiMo/TiO_2 catalyst towards highly efficient hydrodesulfurization reaction. *Catal. Surv. Asia* **2015**, *19*, 1–10. [CrossRef]
21. Xu, P.; Wang, R.; Ouyang, J.; Chen, B. A new strategy for TiO_2 whiskers mediated multi-mode cancer treatment. *Nanoscle Res. Lett.* **2015**, *10*, 94. [CrossRef] [PubMed]
22. He, M.; Lu, X.H.; Feng, X.; Yu, L.; Yang, Z.H. A simple approach to mesoporous fibrous titania from potassium dititanate. *Chem. Commun.* **2004**, *10*, 2202–2203. [CrossRef] [PubMed]

23. Wang, W.Y.; Zhao, X.F.; Ju, X.H.; Wang, Y.; Wang, L.; Li, S.P.; Li, X.D. Novel morphology change of AU-methotrexate conjugates: From nanochains to discrete nanoparticles. *Int. J. Pharm.* **2016**, *515*, 221–232. [CrossRef] [PubMed]
24. Wang, H.; Wang, C.; Bo, X.; Li, Z.; Jian, Z.; Zhu, Y.; Guo, X. The hydroxyapatite nanotube as a promoter to optimize the hds reaction of NiMo/TiO_2 catalyst. *Catal. Today* **2016**, *259*, 340–346. [CrossRef]
25. Shaw, S.S.; Sorbie, K.S. Synergistic properties of phosphonate and polymeric scale-inhibitor blends for barium sulfate scale inhibition. *SPE Prod. Oper.* **2015**, *30*, 16–25. [CrossRef]
26. Alla, E.M.A.; Abdel-Hamid, M.I. Kinetics and mechanism of the non-isothermal decomposition. Some Ni(ii)-carboxylate-imidazole ternary complexes. *J. Therm. Anal. Calorim.* **2000**, *62*, 769–780. [CrossRef]
27. Liu, H.; Cui, Y.; Li, P.; Zhou, Y.; Chen, Y.; Tang, Y.; Lu, T. Polyphosphonate induced coacervation of chitosan: Encapsulation of proteins/enzymes and their biosensing. *Anal. Chim. Acta* **2013**, *776*, 24–30. [CrossRef] [PubMed]
28. Oshani, F.; Marandi, R.; Rasouli, S.; Farhoud, M.K. Photocatalytic investigations of TiO_2–P25 nanocomposite thin films prepared by peroxotitanic acid modified sol–gel method. *Appl. Surf. Sci.* **2014**, *311*, 308–313. [CrossRef]
29. Bun, H.; Monjanel-Mouterde, S.; Noel, F.; Dur, A.; Cano, J.P. Inhibition properties of self-assembled corrosion inhibitor talloil diethylenetriamine imidazoline for mild steel corrosion in chloride solution saturated with carbon dioxide. *Corros. Sci.* **2013**, *77*, 265–272. [CrossRef]
30. Jie, H.; Xu, Q.; Wei, L.; Min, Y.L. Etching and heating treatment combined approach for superhydrophobic surface on brass substrates and the consequent corrosion resistance. *Corros. Sci.* **2015**, *102*, 251–258. [CrossRef]
31. Mahallati, S.; Saremi, E. An assessment on the mill scale effects on the electrochemical characteristics of steel bars in concrete under DC-polarization. *Cem. Concr. Res.* **2006**, *36*, 1324–1329. [CrossRef]
32. Pour-Ali, S.; Dehghanian, C.; Kosari, A. Corrosion protection of the reinforcing steels in chloride-laden concrete environment through epoxy/polyaniline–camphorsulfonate nanocomposite coating. *Corros. Sci.* **2015**, *90*, 239–247. [CrossRef]
33. Ramezanzadeh, B.; Haeri, Z.; Ramezanzadeh, M. A facile route of making silica nanoparticles-covered graphene oxide nanohybrids (SiO_2-GO); fabrication of SiO-GO/epoxy composite coating with superior barrier and corrosion protection performance. *Chem. Eng. J.* **2016**, *303*, 511–528. [CrossRef]
34. Liu, B.; Fang, Z.G.; Wang, H.B.; Wang, T. Effect of cross linking degree and adhesion force on the anti-corrosion performance of epoxy coatings under simulated deep sea environment. *Prog. Org. Coat.* **2013**, *76*, 1814–1818. [CrossRef]
35. Ramezanzadeh, B.; Ahmadi, A.; Mahdavian, M. Enhancement of the corrosion protection performance and cathodic delamination resistance of epoxy coating through treatment of steel substrate by a novel nanometric sol-gel based silane composite film filled with functionalized graphene oxide nanosheets. *Corros. Sci.* **2016**, *109*, 182–205. [CrossRef]
36. Westing, E.P.M.V.; Ferrari, G.M.; Wit, J.H.W.D. The determination of coating performance with impedance measurements—II. Water uptake of coatings. *Corros. Sci.* **1994**, *36*, 957–977. [CrossRef]
37. Behzadnasab, M.; Mirabedini, S.M.; Esfandeh, M. Corrosion protection of steel by epoxy nanocomposite coatings containing various combinations of clay and nanoparticulate zirconia. *Corros. Sci.* **2013**, *75*, 134–141. [CrossRef]
38. Ghazizadeh, A.; Haddadi, S.A.; Mahdavian, M. The effect of sol–gel surface modified silver nanoparticles on the protective properties of the epoxy coating. *RSC Adv.* **2016**, *6*, 18996–19006. [CrossRef]
39. Wang, G.; Zhu, L.; Liu, H.; Li, W. Zinc-graphite composite coating for anti-fouling application. *Mater. Lett.* **2011**, *65*, 3095–3097. [CrossRef]
40. Abdel-Aal, N.; Sawada, K. Inhibition of adhesion and precipitation of $CaCO_3$ by aminopolyphosphonate. *J. Cryst. Growth* **2003**, *256*, 188–200. [CrossRef]
41. Zhang, Z.; Chen, S.; Li, Y.; Li, S.; Wang, L. A study of the inhibition of iron corrosion by imidazole and its derivatives self-assembled films. *Corros. Sci.* **2009**, *51*, 291–300. [CrossRef]